

1 Description of Bow-Tie Nanoantennas Excited by Localized Emitters 2 Using Conformal Transformation

3 Víctor Pacheco-Peña,^{†,‡} Miguel Beruete,^{†,§} Antonio I. Fernández-Domínguez,[⊥] Yu Luo,^{||}
4 and Miguel Navarro-Cía^{*,‡,¶}

5 [†]Antennas Group—TERALAB and [§]Institute of Smart Cities, Universidad Pública de Navarra, Pamplona 31006, Spain

6 [‡]Optical and Semiconductor Devices Group, Imperial College London, London SW7 2AZ, U.K.

7 [⊥]Departamento de Física Teórica de la Materia Condensada and Condensed Matter Physics Center (IFIMAC), Universidad
8 Autónoma de Madrid, Madrid 28049, Spain

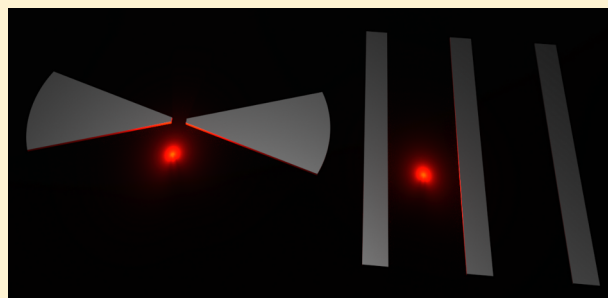
9 ^{||}The Photonics Institute and Centre for OptoElectronics and Biophotonics, School of Electrical & Electronic Engineering, Nanyang
10 Technological University, Singapore 639798, Singapore

11 [#]School of Physics and Astronomy, University of Birmingham, Birmingham B15 2TT, U.K.

12 **S** Supporting Information

13 **ABSTRACT:** The unprecedented advance experienced by nano-
14 fabrication techniques and plasmonics research over the past few
15 years has made possible the realization of nanophotonic systems
16 entering into the so-called strong coupling regime between
17 localized surface plasmon (LSP) modes and quantum emitters.
18 Unfortunately, from a theoretical point of view, the field is
19 hindered by the lack of analytical descriptions of the electro-
20 magnetic interaction between strongly hybridized LSP modes and
21 nanoemitters even within the Markovian approximation. This gap
22 is tackled here by exploiting a conformal transformation where a
23 bow-tie nanoantenna excited by a dipole is mapped into a periodic
24 slab–dipole framework whose analytical solution is available. Solving the problem in the transformed space not only provides a
25 straightforward analytical explanation for the original problem (validated using full-wave simulations) but also grants a deep
26 physical insight and simple design guidelines to maximize the coupling between localized dipoles and the bow-tie LSP modes.
27 The results presented here therefore pave the way for a full analytical description of realistic scenarios where quantum dots or dye
28 molecules (modeled beyond a two-level system) are placed near a metallic bow-tie nanoantenna.

29 **KEYWORDS:** conformal transformation, bow-tie, nanoantenna, plasmonic, transformation optics



30 **A**ntennas are well-known enabling devices for efficient
31 transduction between electronic signals (guided waves)
32 and radio or microwave radiation (nonguided waves).^{1,2} Since
33 their inception at the end of the 19th century, they have been
34 intimately bound to wireless communication systems. However,
35 this view has taken a different perspective in recent years within
36 the field of nanophotonics.³ Benefitting from the recent
37 advances in nanofabrication and optical characterization
38 techniques, as well as the accuracy and predictive value that
39 classical electromagnetics has demonstrated down to the
40 nanoscale, the antenna concept has been revisited in optics.^{4–7}

41 The so-called nanoantennas are devices that operate in the
42 visible range in a similar way to conventional low-frequency
43 antennas. Breaking the diffraction limit of classical optics, these
44 nanometric devices enable near- to far-field coupling (and vice
45 versa) of optical signals with unprecedented efficiency. This
46 nanoscale control over the propagation and confinement of
47 visible light has already found applications in areas completely
48 different from the traditional wireless communications such as

spectroscopy,⁸ biosensing,⁹ photovoltaics,¹⁰ optoelectronics,¹¹
49 photodetection,¹² and nonlinear optics.¹³ 50

51 Like radio and microwave antennas, the electromagnetic
52 response of nanoantennas is governed by their geometries and
53 by the material properties of their components.¹ However,
54 metals have a more complex description at visible frequencies,
55 making the modeling and optimization of these nanodevices
56 more challenging from a theoretical perspective. Hence, the
57 analytical description of nanoantenna performance exists only
58 for a few simple geometries, such as spheres, cylinders, or
59 cuboids.^{14,15} Very recently, a quasi-analytical treatment of more
60 complex nanostructures has been developed using trans-
61 formation optics,^{16–20} a framework similar to conformal
62 mapping^{21–24} but operating exactly at the level of Maxwell
63 equations.²⁵

64 Bow-tie nanoantennas are composed by two triangular-
65 shaped metal nanoparticles facing against each other, connected

Received: April 4, 2016

66 at their apexes or separated by a nanometric gap. This is one of
 67 the most thoroughly investigated structures in the literature.
 68 Experimental and numerical reports have shown the suitability
 69 of this antenna and its variations for the implementation of
 70 optical receivers and transmitters.^{26–34} Compared to the other
 71 geometries examined under transformation optics such as
 72 crescents and cylindrical dimers,²⁰ bow-tie nanoantennas
 73 promise a stronger degree of field localization and enhance-
 74 ment. This benefits and is indeed essential for a myriad of
 75 plasmonic applications; for instance, the stronger the local field,
 76 the brighter the fluorescence/harmonic signal is or the larger
 77 the Rabi splitting of molecular resonance peaks is in hybrid
 78 metal-molecule/nonlinear-material scenarios. In this work, we
 79 extend the set of nanoantenna configurations with analytical
 80 treatment including a two-dimensional bow-tie geometry
 81 (presenting translational symmetry along one direction, as
 82 shown in Figure 1). We exploit transformation optics concepts

simplicity, the bow-tie geometries are embedded in a vacuum, 108
 and the dielectric function of Ag is taken from Palik's 109
 experimental data (see the Methods section for more details 110
 of the numerical study).³⁶ 111

The system can be qualitatively explained with a simple 112
 heuristic analysis. The radiation from the localized oscillating 113
 dipole (an atom or a quantum dot in an excited state, for 114
 instance) is coupled to the different LSP modes supported by 115
 the bow-tie nanoantennas. This pumped electromagnetic 116
 energy is eventually dissipated due to metal absorption, i.e., 117
 nonradiative damping. Given the subwavelength size of the 118
 bow-tie, radiation loss, i.e., radiative damping, is negligible. The 119
 strength of the coupling, and, thus, the nonradiative damping, 120
 depends on the position of the dipole within the field 121
 distribution of the LSP modes. In general, the problem of 122
 finding the optimum set of parameters for a specific experiment 123
 is addressed by performing brute-force computations. An 124
 alternative to reduce the computational requirements is 125
 devising analytical solutions. In the next section we derive a 126
 conformal mapping solution for the bow-tie nanoantenna 127
 excited by a dipole. We transform the problem into a geometry 128
 that can be easily solved analytically, simplifying the calculation 129
 and analysis of the original problem. 130

Theoretical Analysis: Conformal Mapping. The bow tie 131
 can be transformed into the multislab geometry shown in 132
 Figure 1b by applying the following conformal transformation: 133

$$z = \ln(z') \quad (1)$$

where $z = x + iy$ and $z' = x' + iy'$ are the spatial coordinates in 135
 the transformed and original frame, respectively. Through this 136
 conformal transformation, circular (radial) lines in the original 137
 geometry are mapped into vertical (horizontal) lines in the 138
 transformed frame.^{16,30} This transformation results in a 139
 multislab geometry with the dimensions of all metal slabs as 140
 $L_1 + L_2$ and $\theta (= d_3)$ along the x - and y -axis, respectively. The 141
 original dipole is meanwhile converted into an array of dipoles 142
 with the same strength placed along the y -axis with a periodicity 143
 2π , i.e., at $(x = 0, y = 2\pi m)$, where m is an integer. It is worth 144
 pointing out that a scenario involving a nanoantenna with three 145
 arms would be converted into a multislab geometry with an 146
 additional slab per period (see Supporting Information). 147

By looking at the multislab geometry, a qualitative and 148
 quantitative (detailed next) understanding of the LSP modes 149
 supported by the bow-tie nanoantenna can be achieved. As 150
 shown in Figure 1b, the dipole array emission triggers surface 151
 plasmons propagating along both positive and negative 152
 directions of x in the multislab geometry, which are mapped 153
 into the plasmonic modes excited by the single emitter along 154
 both arms of the bow-tie nanoantenna. Because of the finite 155
 length of the slab/bow-tie-arms, these surface plasmons are 156
 reflected back and forth between the two ends of the structure, 157
 forming a standing wave pattern that gives rise to the LSP 158
 modes. Hence, the continuous surface plasmon polariton 159
 spectrum of an infinite slab or bow tie is converted into a finite 160
 set of discrete LSPs, characterized by the mode order n ^{37,38} (see 161
 the Methods section and Supporting Information). 162

The 2D conformal transformation ensures that the material 163
 properties remain unchanged, unlike the 3D counterpart.^{17–20} 164
 In addition, it preserves the potential in each coordinate 165
 system:³⁷ 166

$$\phi(x, y) = \phi'(x', y') \quad (2)$$

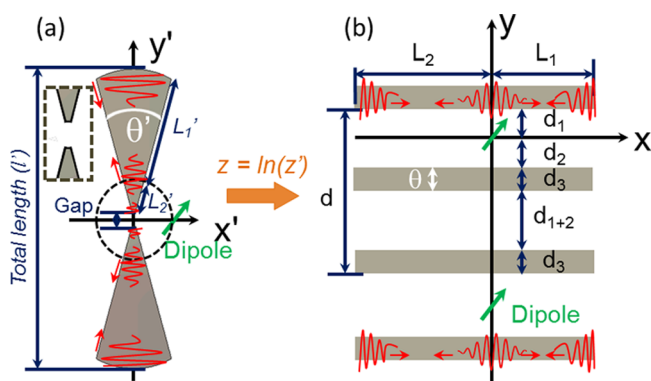


Figure 1. (a) Schematic representation of a metallic bow-tie nanoantenna with a gap on its center illuminated with a dipole placed at $(x', y') = (1 \text{ nm}, 0)$ (green arrow). (b) Transformed geometry after the conformal mapping is applied to the bow-tie nanoantenna.

83 to explain the dependence of the nonradiative decay spectra 84
 (i.e., the power absorbed, P_{abs} , by the bow-tie nanoantenna 85
 under dipole illumination^{20,35}) on the bow-tie geometrical 86
 parameters and to give physical insights on the coupling 87
 between oscillating classical line dipoles and the localized 88
 surface plasmon (LSP) modes supported by the bow-tie 89
 geometry.

90 ■ RESULTS AND DISCUSSION

91 Figure 1a shows the general problem under consideration: the 92
 coupling between a line dipole (nanoemitter) with arbitrary 93
 orientation and a bow-tie nanoantenna made of silver (Ag). 94
 Notice that the tip of the bow-tie nanoantenna studied here is 95
 concave to facilitate the conformal mapping. The dipole is 96
 located on the x' -axis 1 nm away from the center of the bow-tie. 97
 This is indeed a more realistic situation than placing the dipole 98
 inside the gap, since nanometer-size gaps are in general 99
 inaccessible for nano- and micrometer-size emitters. The bow- 100
 tie is defined by the arm length, $L_1' + L_2'$, the arm angle, θ' , and 101
 the gap between arms. The arm length along with the gap gives 102
 the total length of the bow tie, l' . We restrict the study to bow- 103
 tie geometries much smaller than the illumination wavelength 104
 to be within the realm of near-field (quasi-static) approx- 105
 imation. In this scenario, magnetic and electric fields are 106
 decoupled, and the latter can be fully described by an 107
 electrostatic potential satisfying Laplace's equation. For

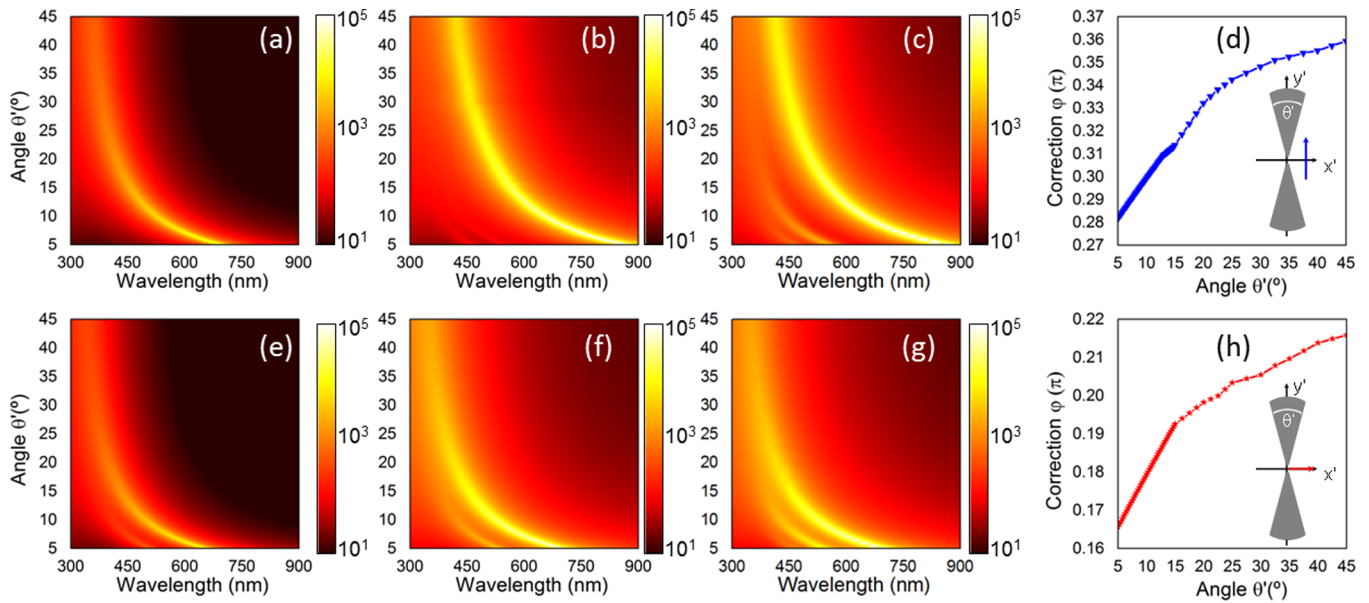


Figure 2. Nonradiative Purcell enhancement spectra as a function of the bow-tie angle θ' for a dipole with vertical (a–d) and horizontal orientation (e–h): analytical results without (a, e) and with correction (b, f) to fit simulation results (c, g). Phase correction applied in the analytical calculations for a dipole with vertical (d) and horizontal (h) polarization.

168 where ϕ and ϕ' are the electrostatic potentials in the
 169 transformed and original frames, respectively. Therefore, the
 170 x' and y' components of the electric field distribution ($E'_{x'}$ and
 171 $E'_{y'}$, respectively) in the original geometry can be directly
 172 deduced from eq 2 as^{38,39}

$$173 \quad E'_{x'} = -\frac{\partial\phi'}{\partial z'} \frac{\partial z}{\partial x'} - \frac{\partial\phi'}{\partial z'^*} \frac{\partial z'^*}{\partial x'} = -\frac{\partial\phi'}{\partial z'} - \frac{\partial\phi'}{\partial z'^*} \quad (3)$$

$$174 \quad E'_{y'} = -\frac{\partial\phi'}{\partial z'} \frac{\partial z}{\partial y'} - \frac{\partial\phi'}{\partial z'^*} \frac{\partial z'^*}{\partial y'} = -i\frac{\partial\phi'}{\partial z'} + i\frac{\partial\phi'}{\partial z'^*} \quad (4)$$

175 Hence, by solving the problem in the multislabs frame, the
 176 bow-tie scenario is solved straightforwardly. Notice that, in the
 177 multislabs geometry, the field distribution along the y direction
 178 (E_y) actually represents the azimuthal component of the electric
 179 field ($E'_{\phi'}$) in the bow-tie scenario, which can be calculated
 180 from the x' and y' components (eqs 3 and 4) as $E'_{\phi'} = -E'_{x'}$
 181 $\sin(\varphi') + E'_{y'} \cos(\varphi')$, with $\varphi' = \tan^{-1}(y'/x')$. On the other
 182 hand, the field distribution along the x direction (E_x) is directly
 183 transformed into the radial component of the electric field in
 184 the original geometry ($E'_{\rho'}$), which can be obtained as $E'_{\rho'} =$
 185 $E'_{x'} \cos(\varphi') + E'_{y'} \sin(\varphi')$. From here on, the azimuthal and
 186 radial components will be used to represent the electric field
 187 distribution in the bow-tie nanoantennas here studied. The
 188 quantitative details of the analytical formulation to calculate the
 189 plasmonic response of the bow-tie nanoantenna are derived in
 190 the Methods section, where the problem is solved for the
 191 multislabs geometry.

192 Nonradiative Decay in the Gap Bow-Tie Nanoantenna.

193 Since the energy is conserved in the transformation, the power
 194 dissipation is the same in both frames. Hence, the nonradiative
 195 decay of the nanoemitter can be deduced by calculating the
 196 power dissipated in the multislabs geometry. This can be
 197 obtained by evaluating the electric field at the dipole position in
 198 the original frame, as follows:

$$P_{\text{nr}} = P_{\text{abs}} = -\frac{1}{2}\omega \text{Im}\{p_x E'_{1x}(x, y=0) + p_y E'_{1y}(x, y=0)\} \quad (5) \quad 199$$

where P_{nr} is the nonradiative power emission, $\omega = 2\pi c/\lambda_0$ is the
 200 angular frequency at the working wavelength λ_0 , c is the velocity
 201 of light in a vacuum, p_x and p_y are the components of the dipole
 202 moment along the x and y directions, and E'_{1x} and E'_{1y} are the
 203 components of the electric field along the x and y directions in
 204 the region where the dipole is placed ($d_2 < y < d_1$). Importantly,
 205 in our calculations, an intrinsic quantum yield equal to 1 is
 206 assumed for the nanoemitter, which allows identifying the
 207 nonradiative decay experienced by the emitter and the power
 208 absorbed by the bow-tie nanoantenna.⁴⁰ Moreover, note that as
 209 eq 5 is derived in the quasi-static approximation, the expression
 210 for the extinguished power by a point dipole can be used to
 211 describe the nanoemitter nonradiative decay. 212

213 Plasmonic Response of Gap Bow-Tie Nanoantennas.

214 *Changing the Bow-Tie Arm Angle.* Let $\Gamma_0(\omega)$ and $\Gamma_{\text{nr}}(\omega)$ be
 215 the isolated dipole radiative rate and the nonradiative decay rate
 216 for the full system. Figure 2 renders the evolution of the
 217 nonradiative Purcell enhancement rate spectra $\Gamma_{\text{nr}}(\omega)/\Gamma_0(\omega)$
 218 (calculated as the ratio of the power absorbed by the
 219 nanoparticle P_{nr} and the total power radiated by the isolated
 220 localized emitter P_0 , i.e., $\Gamma_{\text{nr}}(\omega)/\Gamma_0(\omega) = P_{\text{nr}}/P_0$)^{3,20,35} as a
 221 function of θ' for a bow-tie nanoantenna with total length $l' =$
 222 20 nm and a normalized gap between both arms of 0.05 l' . The
 223 analytical results are evaluated using eq 5 along with the power
 224 radiated by the dipole, $P_0 = (1/16)(\omega^3\mu_0)(|p|^2)$, with μ_0 the
 225 permeability of the vacuum and $|p|$ the magnitude of the dipole
 226 moment, respectively. The analytical results are compared with
 227 numerical calculations done with the commercial software
 228 Comsol Multiphysics (see the Methods section). The analytical
 229 results for the vertically oriented dipole case (Figure 2a) show
 230 that the maximum of $\Gamma_{\text{nr}}(\omega)/\Gamma_0(\omega)$ shifts from ~ 698 nm to
 231 ~ 394 nm when the angle θ' varies from 5° to 45° . This peak
 232 originates from the first ($n = 1$) LSP mode supported by the
 233 bow-tie nanoantenna, as we show below through the field
 234 distribution inspection. Similarly, for a horizontal dipole, the

235 first nonradiative peak due to the first LSP mode is blue-shifted
 236 from ~ 650 nm to ~ 337 nm; see Figure 2e. Although similar
 237 trends are observed in the full-wave simulations, there is an
 238 evident blue-shift between simulation results (Figure 2c,g) and
 239 analytical calculations for both dipole orientations (Figure
 240 2a,e). The blue-shift arises from the assumption that the LSP
 241 modes acquire a phase shift of π upon reflection at each end of
 242 the metal slabs, i.e., at the open boundaries (at L_1 and $-L_2$). To
 243 account for a different reflection phase shift, a correction is
 244 introduced in the form of an extra phase $\Delta\varphi$. The calculation of
 245 $\Delta\varphi$ is done by fitting the analytically computed wavelength of
 246 the fundamental mode ($n = 1$ LSP mode) to the simulations.
 247 Since higher order LSP modes may experience different
 248 reflection conditions than the fundamental one, this correction
 249 may not apply for higher order modes. The values of $\Delta\varphi$ for a
 250 vertical and horizontal dipole as a function of the angle θ' are
 251 shown in Figure 2d,h, respectively. A linear slope is obtained for
 252 angles from 5° to 15° , while this tendency varies for larger
 253 angles. The corrected $\overline{\Gamma}_{\text{nr}}(\omega)/\Gamma_0(\omega)$ is shown in Figure 2b,f for
 254 a vertical and horizontal dipole, respectively. Now, a good
 255 agreement between analytical and numerical results is obtained.
 256 As explained before, due to the finite size of the bow-tie
 257 nanoantennas (and the equivalent transformed problem), the
 258 LSPs are distributed as a set of discrete modes in the spectra.
 259 The resonant condition of these discrete LSP modes and their
 260 spectral distribution are provided in the Supporting Informa-
 261 tion for several bow-tie angles excited by both vertical and
 262 horizontal dipoles. From now on, $\overline{\Gamma}_{\text{nr}} = \Gamma_{\text{nr}}(\omega)/\Gamma_0(\omega)$ will refer
 263 to the corrected results.

264 Next, we analyze in detail the analytical and simulation
 265 results of the nonradiative Purcell enhancement spectra for two
 266 bow-tie nanoantennas with $\theta' = 5^\circ$ and 30° excited by a vertical
 267 (Figure 3a) and horizontal dipoles (Figure 3b). Letting $\Gamma_r(\omega)$
 268 be the radiative decay rate for the full system, the simulation
 269 results of the radiative Purcell enhancement $\overline{\Gamma}_r = \Gamma_r(\omega)/\Gamma_0(\omega)$

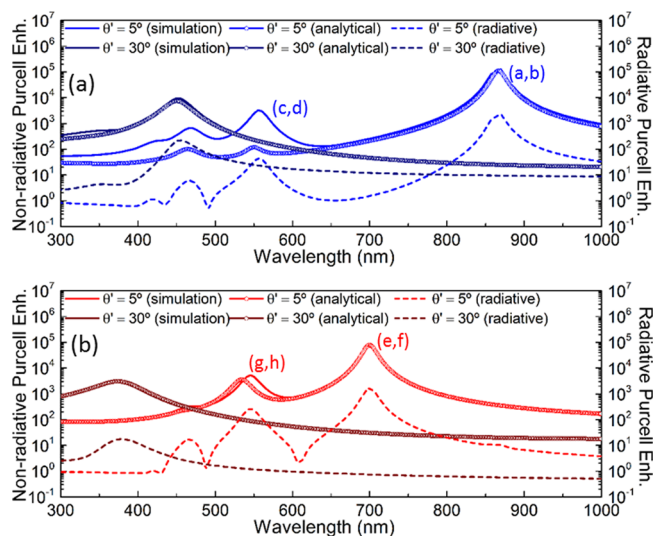


Figure 3. Analytical (dots) and simulation (solid lines) results of the nonradiative Purcell enhancement spectra along with the simulation results of the radiative Purcell enhancement spectra (dashed lines) for two bow ties with angles $\theta' = 5^\circ$ (light lines) and $\theta' = 30^\circ$ (dark lines) when a vertical (a) and horizontal (b) dipole is used as a radiative source. The letters next to the peaks refer to the different panels in Figure 4.

(calculated as the ratio of the power radiated by the system 270
 enclosed by the nanoparticle-dipole P_r and P_0 ; $\Gamma_r(\omega)/\Gamma_0(\omega) =$ 271
 P_r/P_0)^{3,20,35} are also shown in the same figure for completeness. 272
 Notice that it is consistently at least 2 orders of magnitude 273
 smaller than $\overline{\Gamma}_{\text{nr}}$ and thus negligible, as we assumed initially. A 274
 good quantitative agreement between analytical and numerical 275
 results is shown in Figure 3a,b for the first nonradiative peak, 276
 while the other peaks are slightly blue-shifted, as expected from 277
 the above discussion on $\Delta\varphi$. An average blue-shift of 0.9% and 278
 2% is observed between the simulation and analytical results for 279
 the peak associated with the $n = 2$ LSP mode for the bow-tie 280
 nanoantenna with $\theta' = 5^\circ$ for a vertical and horizontal dipole, 281
 respectively. 282

The simulation results of $\overline{\Gamma}_{\text{nr}}$ and $\overline{\Gamma}_r$ along with the 283
 absorption cross sections of the bow-tie nanoantennas under 284
 plane-wave illumination are shown in the Supporting 285
 Information. 286

Figure 4 shows the spatial absorption profiles across the bow- 287 f4
 tie nanoantenna with $\theta' = 5^\circ$ and different dipole orientations 288

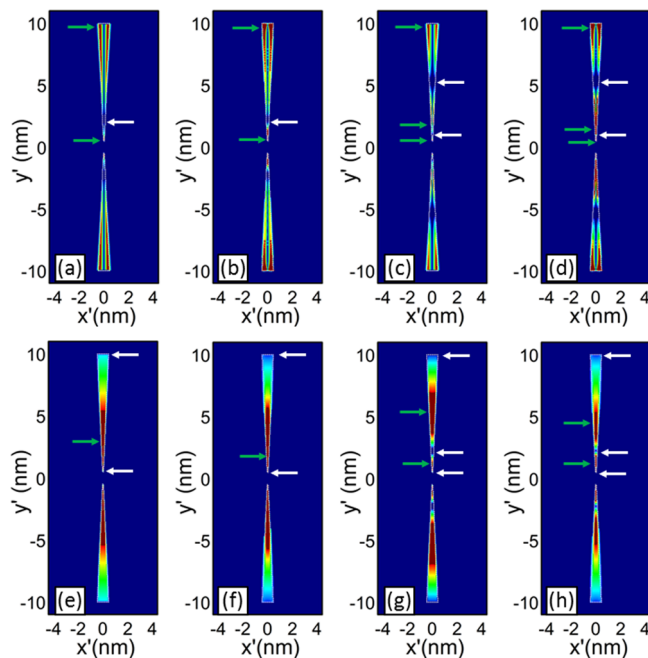


Figure 4. Analytical (a, c, e, g) and simulation-computed (b, d, f, h) absorption for the bow tie with angle $\theta' = 5^\circ$ when the illuminating dipole is vertical (top) and horizontal (bottom): fundamental (a, b, e, f) and second nonradiative decay rate peak (c, d, g, h) within the spectral window of interest. The scale color bar is saturated for clarity. Horizontal green and white arrows indicate the location of respectively the maxima and minima on the top arm of each bow tie.

calculated at the wavelengths highlighted in Figure 3. The same 289
 results for $\theta' = 30^\circ$ can be found in the Supporting Information. 290
 A good agreement between analytical and simulation results is 291
 noticed. As expected, when several absorption maxima exist, the 292
 absolute one is obtained closer to the apices for all cases. This 293
 is a consequence of the larger field concentration close to the 294
 gap, which happens due to the spatial compression of the 295
 surface plasmon modes.³⁰ The spatial absorption distribution 296
 for the fundamental mode under a vertical dipole illumination 297
 (Figure 4a,b) has an absorption minimum pointed out by white 298
 horizontal arrows at $y' = 2.2$ nm ($y' = 2.36$ nm) in the analytical 299
 (numerical) calculation. This absorption minimum represents 300

301 the node of the $n = 1$ LSP mode. For the peaks associated with
 302 the $n = 2$ LSP mode, Figure 4c,d, one can however notice a
 303 local maximum at $y' = 2.06$ nm ($y' = 1.8$ nm) in the analytical
 304 (numerical) results located at each arm of the bow-tie
 305 nanoantenna, pointed out by horizontal green arrows. This
 306 occurs because this position corresponds to the antinode of the
 307 $n = 2$ LSP mode. Under horizontal dipole illumination, the
 308 positions of the maxima and minima change according to the
 309 antinodes of the corresponding LSP modes, as demonstrated
 310 next through electric field distribution patterns. Therefore, the
 311 bow-tie nanoantennas investigated here have a multiband
 312 absorption response that arises from the efficient coupling of
 313 the localized emitter to the multiple LSP modes supported
 314 within the range from 300 to 900 nm.

315 A snapshot of the field distribution for a bow-tie nano-
 316 antenna with $\theta' = 5^\circ$ is shown in Figure 5 for the first and

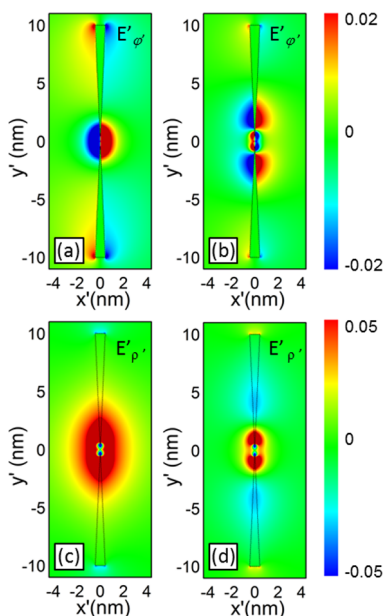


Figure 5. Snapshot of $E'_{\phi'}$ field (top row) and $E'_{\rho'}$ field (bottom row) for a bow-tie nanoantenna with angle $\theta' = 5^\circ$ and illuminated with a vertical (a, b) and a horizontal (c, d) dipole at the peaks in Figure 3: (a) 869 nm, (b) 556 nm, (c) 698 nm, and (d) 545 nm. Note that the scale bar has been saturated from -0.02 to 0.02 and from -0.05 to 0.05 to better appreciate the field distribution across the whole space.

317 second peak of $\overline{\Gamma}_{nr}$ of each dipole orientation. For convenience,
 318 here we plot $E'_{\phi'}$ and $E'_{\rho'}$ for the vertical and horizontal dipole
 319 excitation, respectively. From these color plots we can clearly
 320 identify the mode order of the various LSPs. Under a vertical
 321 dipole illumination, the azimuthal field distribution at the first
 322 $\overline{\Gamma}_{nr}$ peak has a null between the field maxima at the edges of
 323 each bow-tie arm (Figure 5a). For the second peak (Figure 5b),
 324 we have three antinodes and two nulls along the radial direction
 325 in each arm, which corresponds to the $n = 2$ LSP mode. On the
 326 other hand, for the case of a horizontally oriented emitter, two
 327 minima appear at both ends of each arm with an antinode
 328 between them at the lowest $\overline{\Gamma}_{nr}$ peak (Figure 5c), which
 329 corresponds to the $n = 1$ LSP mode. At the second peak
 330 (Figure 5d) the field distribution can be linked to the $n = 2$ LSP
 331 mode, as it has three nulls (one at the center and two at the
 332 extremes of each arm) and two maxima in between
 333 consecutive nulls. Notice that the electric field is stronger at

the antinodes near the apex of the bow ties, as expected from
 the spatial absorption profiles. Alternatively, the field
 distribution can be easily associated with standing wave
 patterns in the transformed frame, as elaborated in the
 Supporting Information.

Changing the Gap of the Bow-Tie Nanoantenna. All the
 results discussed in the previous sections have been obtained
 considering bow-tie nanoantennas with varying θ' . We discuss
 next the influence of the gap size in the nonradiative spectra of
 two bow-tie nanoantennas with $\theta' = 5^\circ$, for a fixed antenna
 length ($l' = 20$ nm). The Supporting Information contains the
 results for $\theta' = 30^\circ$. The analytical results for $\overline{\Gamma}_{nr}$ as a function
 of the gap distance between both arms are shown in the first
 row of Figure 6 when a vertical (Figure 6a) and a horizontal
 (Figure 6b) dipole is placed at $x' = 1$ nm, $y' = 0$ nm. It can be
 observed that all peaks (related to a specific LSP mode) for
 both polarizations and angles are blue-shifted when the gap is
 increased. This blue-shift can be easily explained in terms of the

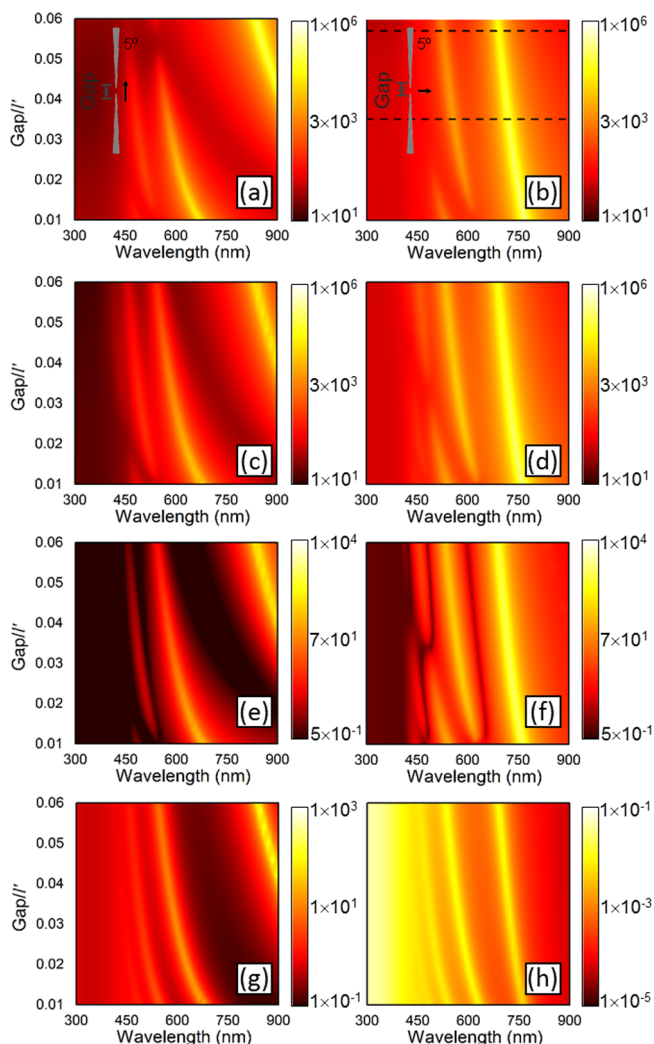


Figure 6. Analytical (first row) and simulated (second row) nonradiative Purcell enhancement spectra along with the simulation results of the radiative Purcell enhancement spectra (third row) and absorption cross section (fourth row) as a function of the gap between the arms of the bow tie with angle $\theta' = 5^\circ$ when a vertically (first column) and horizontally (second column) polarized dipole (top three rows) or plane-wave is used as a source (bottom row).

transformed multislabs geometry: an increment of the gap between both arms of the bow-tie nanoantenna is equivalent to reducing the total length of the slabs in the transformed frame (i.e., $L = L_1 + L_2$ is reduced). Hence, the resonant condition (of the standing wave pattern) happens for shorter wavelengths.

To facilitate the description and comparison, the corresponding numerical spectra are shown in the second row of Figure 6. These panels demonstrate a very good agreement with the analytical results. For $\theta' = 5^\circ$ and a vertical dipole (Figure 6a,c) the \overline{T}_{nr} peak related to the $n = 1$ LSP mode is blue-shifted from ~ 1132 nm (not shown) to ~ 845 nm when the normalized gap goes from $0.01l'$ to $0.06l'$. Interestingly, this peak is not always the \overline{T}_{nr} absolute maximum, in contrast to what happens for the absorption cross section for a bow tie under plane-wave illumination (shown in the bottom row of Figure 6). For instance, \overline{T}_{nr} is larger for the $n = 2$ LSP mode for a normalized gap of $0.01l'$. This shows that there are preferred positions to increase the transfer of energy from the radiative dipole source to the different LSP modes. In particular, for the case $0.01l'$, the vertical dipole is located at a field distribution null of the $n = 1$ LSP eigenmode (not shown here). Hence the peak associated with this mode vanishes. For the case of a horizontal dipole (Figure 6b,d) the peak due to the $n = 1$ LSP mode is blue-shifted from ~ 769 nm to ~ 697 nm when the normalized gap is increased from $0.01l'$ to $0.06l'$. The two other nonradiative peaks (related to the $n = 2$ and $n = 3$ LSP modes, respectively) are also blue-shifted as the gap is increased. Here, the analytical \overline{T}_{nr} peaks due to the second and third higher order mode are also blue-shifted from simulation results by an averaged percentage of 1.1% and 1.37%, respectively, for a vertical dipole and 1.67% and 1.2% for a horizontal dipole. The blue-shift is smaller for a horizontal dipole because of the comparatively shorter phase correction applied to this configuration.

As has been described before, depending of the angle θ' , gap, and orientation of the dipole, the localized emitter cannot transfer energy efficiently to the LSP modes (displayed as minima in the nonradiative Purcell enhancement). This phenomenon can be easily explained by looking at the multislabs geometry. Let us then analyze the case of the bow tie with $\theta' = 5^\circ$ illuminated with a horizontal dipole (Figure 6b,d, analytical and simulation results, respectively). It can be observed that there is a range of gaps between $\sim 0.028l'$ and $\sim 0.038l'$ where the peak linked to the $n = 3$ LSP mode vanishes. To investigate in detail this feature, the \overline{T}_{nr} for this bow-tie nanoantenna using a horizontal dipole is shown in Figure 7a,e for a normalized gap of $0.057l'$ and $0.035l'$, respectively (these panels have been extracted from the black dashed lines of Figure 6b). For the case of a gap of $0.057l'$, Figure 7a shows that three peaks are present at ~ 691 , ~ 522 , and ~ 454 nm, which are those related to the LSP modes with $n = 1, 2$, and 3 , respectively. On the other hand, when the gap is $0.035l'$ (Figure 7e) all peaks are red-shifted, as expected, to ~ 721 , ~ 556 , and ~ 433 nm. Nevertheless, the LSP mode with $n = 3$ at ~ 433 nm almost disappears.

This phenomenon can be explained by analyzing the fields in the transformed geometry, as follows: first, the analytical results of the normalized magnitude of the electric field distribution in the multislabs geometry for the case of a gap of $0.057l'$ at the first, second, and third peaks are shown in Figure 7b–d, respectively. The field distribution at these peaks corresponds to the field distribution of the LSP modes with $n = 1, 2$, and 3 ,

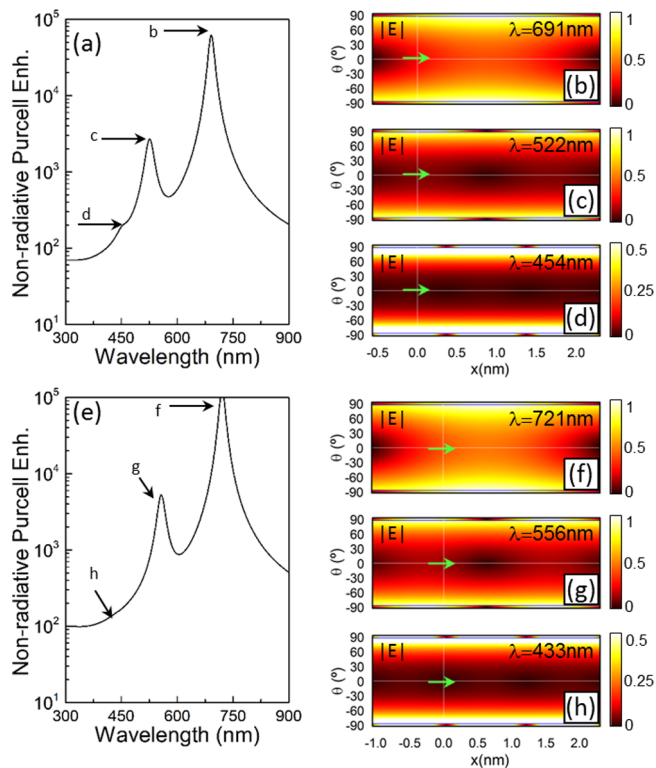


Figure 7. Analytical nonradiative Purcell enhancement spectra for a bow tie with $\theta' = 5^\circ$ and gap = $0.057l'$ (a) and $0.035l'$ (e). Analytical normalized magnitude of the electric field for the parallel-plate geometry at the relevant spectral position shown in (a) and (e). The position of the illuminating horizontal dipole is shown as a green arrow for clarity. Note that the scale in (d) and (h) has been saturated from 0 to 0.5 to better observe the field distribution.

respectively, as it has been explained before. For the case of the first LSP mode ($n = 1$) the horizontal dipole (schematically shown as a horizontal green arrow) is placed close but not just at the node at $-L_2$ (i.e., the node in the standing wave pattern) of the field distribution; therefore, the dipole can couple to this LSP mode. However, for $n = 2$ (Figure 7c) the dipole is closer to the first node, where poorer transfer of energy between the dipole to the LSP is expected. Hence, a reduction of \overline{T}_{nr} takes place for this mode compared to the first one. Similar performance can be observed for $n = 3$. In this case, the dipole is even closer to the node compared with the first and second modes; therefore, the amplitude of the peak is reduced, although it still appears in the spectrum. Now, let us analyze the case when the gap is $0.035l'$. For this geometry, the normalized magnitude of the electric field at 721, 556, and 433 nm is shown in Figure 7f–h, respectively. As it can be observed in Figure 7h, the field distribution corresponds to the LSP mode with $n = 3$, as explained before. Moreover, it is shown that the horizontal dipole is exactly at the position where the distribution of the electric field has a node. Therefore, the electromagnetic energy released by the dipole does not couple efficiently to this LSP mode, giving rise to a null in \overline{T}_{nr} . On the contrary, for the case of the first and second peaks (see Figure 7f,g, respectively) the horizontal dipole is located at a more favorable position for energy transfer to the LSP modes than for the $n = 3$ LSP mode and the $n = 1$ and 2 LSP modes for a $0.057l'$ gap; hence, the nonradiative decay rate is higher for them.

440 ■ CONCLUSIONS

441 In conclusion, an analytical solution for bow-tie nanoantennas
 442 based on conformal transformation in the quasi-static
 443 approximation has been rigorously derived. For situations
 444 beyond the quasi-static limit, one could explore the
 445 implementation of a radiative correction based on a fictitious
 446 absorbing dipole in the transformed space.^{20,38} The conformal
 447 transformation permits converting the original problem of a
 448 bow-tie nanoantenna excited by a local dipole into a multislabs
 449 geometry with an array of dipoles whose solution can be found
 450 analytically and is also the solution of the original bow-tie
 451 nanoantenna scenario. Our conformal mapping approach also
 452 enables us to describe in detail all the spectral features in the
 453 nonradiative Purcell enhancement of a nanoemitter placed in
 454 the vicinity of different bow-tie nanoantennas. These results
 455 should ease the design of bow-tie nanoantennas for multiple
 456 applications. In particular, it may hold promise to model
 457 analytically the dynamics of realistic strong coupling scenarios
 458 where localized surface plasmon modes interact with states
 459 linked to few-level emitters such as quantum dots or dye
 460 molecules.

461 ■ METHODS

462 **Multislabs Geometry Mimicking the Gap Bow-Tie**
 463 **Nanoantenna.** Here, the multislabs geometry shown in Figure
 464 1b is solved. Taking into account that the dimensions of the
 465 bow-tie nanoantenna are sufficiently smaller than the opera-
 466 tional wavelength ($l \ll \lambda_0$), the near-field approximation can
 467 be used, and thus, the electric field can be fully described by an
 468 electrostatic potential satisfying Laplace's equation. As it is
 469 known, in the multislabs geometry shown in Figure 1b, it is
 470 possible to excite surface plasmon modes in both transversal
 471 and longitudinal directions, with their propagation along the x -
 472 and y -axis, respectively. However, the interest here is focused in
 473 the derivation of the surface plasmon modes excited in the
 474 multislabs geometry when $L_1 + L_2 \gg \theta$; thereby, the
 475 contribution of the longitudinal LSP modes (i.e., those with
 476 phase variation along y) can be neglected and it can be assumed
 477 that the excited LSP modes are mainly due to the transversal
 478 modes (i.e., those with phase variation along x). On this basis,
 479 the electrostatic potentials outside and inside the metal strips in
 480 Figure 1b can be calculated as a sum of all discrete transverse
 481 modes, as follows:

$$482 \sum_k \left[\frac{1}{1 - e^{2ik(L_1+L_2)+2i\Delta\varphi}} (e^{ikx} + e^{-ikx+2ikL_1+i\Delta\varphi}) \right. \\ \left. \times (A_+ e^{-ky} + B_+ e^{-ky} + B_- e^{ky}) \right], 0 < y < d_1 \quad (6)$$

$$483 \sum_k \left[\frac{1}{1 - e^{2ik(L_1+L_2)+2i\Delta\varphi}} (e^{ikx} + e^{-ikx+2ikL_1+i\Delta\varphi}) \right. \\ \left. \times (A_- e^{ky} + B_+ e^{-ky} + B_- e^{ky}) \right], -d_2 < y < 0 \quad (7)$$

$$\sum_k \left[\frac{1}{1 - e^{2ik(L_1+L_2)+2i\Delta\varphi}} (e^{ikx} + e^{-ikx+2ikL_1+i\Delta\varphi}) \right. \\ \left. \times (E_+ e^{-ky} + E_- e^{ky}) \right], -(d_1 + 2d_2 + d_3) < y \\ < -(d_2 + d_3) \quad (8) \quad 484$$

$$\sum_k \left[\frac{1}{1 - e^{2ik(L_1+L_2)+2i\Delta\varphi}} (e^{ikx} + e^{-ikx+2ikL_1+i\Delta\varphi}) \right. \\ \left. \times (C_+ e^{-ky} + C_- e^{ky}) \right], -(d_1 + 2d_2 + 2d_3) < y \\ < -(d_1 + 2d_2 + d_3) \quad (9) \quad 485$$

$$\sum_k \left[\frac{1}{1 - e^{2ik(L_1+L_2)+2i\Delta\varphi}} (e^{ikx} + e^{-ikx+2ikL_1+i\Delta\varphi}) \right. \\ \left. \times (D_+ e^{-ky} + D_- e^{ky}) \right], -(d_2 + d_3) < y < -d_2 \quad (10) \quad 486$$

where k is the wave vector of the transverse LSP modes
 487 calculated as $k = (n\pi - \Delta\varphi)/(L_1 + L_2)$ with $n = 1, 2, 3, \dots$,
 488 representing the discrete transverse SP mode, $\Delta\varphi$ is the
 489 correction of phase applied to the bow-tie nanoantenna to take
 490 into account the complex reflection experienced by the surface
 491 plasmon waves at the extremes of the nanoparticle, A_+ and A_-
 492 are the expansion coefficients of the incident potential, B_+ and
 493 B_- are the coefficients related to the scattering potential in the
 494 region where the dipole is placed ($d_2 < y < d_1$), E_+ and E_-
 495 are the coefficients associated with the scattering potential in the
 496 region where a dipole is absent ($d_2 + d_1$), and C_+ , C_- , D_+ , and
 497 D_- are those corresponding to the potential inside the metal
 498 strips (d_3). The coefficients associated with the incident
 499 potential can be obtained by expanding the dipole potential
 500 along the x direction using a Fourier transform: 501

$$A_{\pm} = \frac{\pm p_y - ip_x \operatorname{sgn}(k)}{2\epsilon_0} \quad (11) \quad 502$$

where p_y and p_x are the components of the dipole moment
 503 along the x and y directions, respectively, and ϵ_0 is the
 504 permittivity under vacuum. 505

The other eight unknown coefficients B_+ , B_- , C_+ , C_- , D_+ , D_- ,
 506 E_+ , and E_- can be solved by using the boundary conditions at
 507 each interface of Figure 1b. First, the condition of conservation
 508 of the parallel component of the electric field at the boundaries
 509 d_2 , $d_2 + d_3$, d_1 , and $d_1 + 2d_2 + 2d_3$ is applied, as follows: 510

$$A_- e^{-kd_2} + B_+ e^{kd_2} + B_- e^{-kd_2} = D_- e^{-kd_2} + D_+ e^{kd_2} \quad (12) \quad 511$$

$$E_+ e^{k(d_2+d_3)} + E_- e^{-k(d_2+d_3)} = D_- e^{-k(d_2+d_3)} + D_+ e^{k(d_2+d_3)} \quad (13) \quad 512$$

$$A_+ e^{-kd_1} + B_+ e^{-kd_1} + B_- e^{kd_1} \\ = C_- e^{-k(d_1+2d_2+2d_3)} + C_+ e^{k(d_1+2d_2+2d_3)} \quad (14) \quad 513$$

$$E_+ e^{k(d_1+2d_2+d_3)} + E_- e^{-k(d_1+2d_2+d_3)} \\ = C_- e^{-k(d_1+2d_2+d_3)} + C_+ e^{k(d_1+2d_2+d_3)} \quad (15) \quad 514$$

515 Also, the condition of conservation of the normal component
516 of the displacement field at the same boundaries as eqs 12–15
517 is applied, as follows:

$$518 \quad A_- e^{-kd_2} - B_+ e^{kd_2} + B_- e^{-kd_2} = \varepsilon D_- e^{-kd_2} - \varepsilon D_+ e^{kd_2} \quad (16)$$

$$519 \quad E_+ e^{k(d_2+d_3)} - E_- e^{-k(d_2+d_3)} = -\varepsilon D_- e^{-k(d_2+d_3)} + \varepsilon D_+ e^{k(d_2+d_3)} \quad (17)$$

$$520 \quad A_+ e^{-kd_1} + B_+ e^{-kd_1} - B_- e^{kd_1} \\ = -\varepsilon C_- e^{-k(d_1+2d_2+2d_3)} + \varepsilon C_+ e^{k(d_1+2d_2+2d_3)} \quad (18)$$

$$521 \quad -E_+ e^{k(d_1+2d_2+d_3)} + E_- e^{-k(d_1+2d_2+d_3)} \\ = \varepsilon C_- e^{-k(d_1+2d_2+d_3)} - \varepsilon C_+ e^{k(d_1+2d_2+d_3)} \quad (19)$$

522 where ε is the permittivity of the metal used in the structure
523 (silver in this case). The solutions of the potentials in the real
524 space for the region where there is ($d_2 < y < d_1$) and there is no
525 dipole ($d_2 + d_1$), ϕ_1^s and ϕ_2^s , respectively, can then be obtained
526 by applying an inverse Fourier transform to the induced
527 potentials:

$$\phi_1^s = \frac{1}{2\varepsilon_0(L_1 + L_2)} \sum_n \langle \Theta \{ p_x [\sin(kx) - \sin(kx - 2kL_1 - \Delta\varphi)] \\ + p_y [\cos(kx) + \cos(kx - 2kL_1 - \Delta\varphi)] \} \\ \times (B_+ e^{-ky} + B_- e^{ky}) \rangle \quad (20)$$

$$\phi_2^s = \frac{1}{2\varepsilon_0(L_1 + L_2)} \sum_n \langle \Theta \{ p_x [\sin(kx) - \sin(kx - 2kL_1 - \Delta\varphi)] \\ + p_y [\cos(kx) + \cos(kx - 2kL_1 - \Delta\varphi)] \} \\ \times (E_+ e^{-ky} + E_- e^{ky}) \rangle \quad (21)$$

530 Similarly, the potentials inside both metallic slabs (ϕ_1^m and
531 ϕ_2^m) are

$$\phi_1^m = \frac{1}{2\varepsilon_0(L_1 + L_2)} \sum_n \langle \Theta \{ p_x [\sin(kx) - \sin(kx - 2kL_1 - \Delta\varphi)] \\ + p_y [\cos(kx) + \cos(kx - 2kL_1 - \Delta\varphi)] \} \\ \times (C_+ e^{-ky} + C_- e^{ky}) \rangle \quad (22)$$

$$\phi_2^m = \frac{1}{2\varepsilon_0(L_1 + L_2)} \sum_n \langle \Theta \{ p_x [\sin(kx) - \sin(kx - 2kL_1 - \Delta\varphi)] \\ + p_y [\cos(kx) + \cos(kx - 2kL_1 - \Delta\varphi)] \} \\ \times (D_+ e^{-ky} + D_- e^{ky}) \rangle \quad (23)$$

534 where Θ is defined as

$$\Theta = \frac{1}{\{1 - \cos[2k(L_1 + L_2) + 2\Delta\varphi] - \sin[2k(L_1 + L_2) + 2\Delta\varphi]\}} \quad (24) \quad 535$$

Finally, the x and y components of the electric field can be
536 calculated by simply differentiating the potentials: 537

$$E_{1x}^s = \sum_n -\frac{k}{2\varepsilon_0(L_1 + L_2)} \langle \{ p_x [\cos(kx) - \cos(kx - 2kL_1 - \Delta\varphi)] \\ - p_y [\sin(kx) + \sin(kx - 2kL_1 - \Delta\varphi)] \} (B_+ e^{-ky} + B_- e^{ky}) \rangle \quad (25) \quad 538$$

$$E_{2x}^s = \sum_n -\frac{k}{2\varepsilon_0(L_1 + L_2)} \langle \{ p_x [\cos(kx) - \cos(kx - 2kL_1 - \Delta\varphi)] \\ - p_y [\sin(kx) + \sin(kx - 2kL_1 - \Delta\varphi)] \} (E_+ e^{-ky} + E_- e^{ky}) \rangle \quad (26) \quad 539$$

$$E_{1x}^m = \sum_n -\frac{k}{2\varepsilon_0(L_1 + L_2)} \langle \{ p_x [\cos(kx) - \cos(kx - 2kL_1 - \Delta\varphi)] \\ - p_y [\sin(kx) + \sin(kx - 2kL_1 - \Delta\varphi)] \} (C_+ e^{-ky} + C_- e^{ky}) \rangle \quad (27) \quad 540$$

$$E_{2x}^m = \sum_n -\frac{k}{2\varepsilon_0(L_1 + L_2)} \langle \{ p_x [\cos(kx) - \cos(kx - 2kL_1 - \Delta\varphi)] \\ - p_y [\sin(kx) + \sin(kx - 2kL_1 - \Delta\varphi)] \} (D_+ e^{-ky} + D_- e^{ky}) \rangle \quad (28) \quad 541$$

$$E_{1y}^s = \sum_n -\frac{k}{2\varepsilon_0(L_1 + L_2)} \langle \{ p_x [\sin(kx) - \sin(kx - 2kL_1 - \Delta\varphi)] \\ + p_y [\cos(kx) + \cos(kx - 2kL_1 - \Delta\varphi)] \} (-B_+ e^{-ky} + B_- e^{ky}) \rangle \quad (29) \quad 542$$

$$E_{2y}^s = \sum_n -\frac{k}{2\varepsilon_0(L_1 + L_2)} \langle \{ p_x [\sin(kx) - \sin(kx - 2kL_1 - \Delta\varphi)] \\ + p_y [\cos(kx) + \cos(kx - 2kL_1 - \Delta\varphi)] \} (-E_+ e^{-ky} + E_- e^{ky}) \rangle \quad (30) \quad 543$$

$$E_{1y}^m = \sum_n -\frac{k}{2\varepsilon_0(L_1 + L_2)} \langle \{ p_x [\sin(kx) - \sin(kx - 2kL_1 - \Delta\varphi)] \\ + p_y [\cos(kx) + \cos(kx - 2kL_1 - \Delta\varphi)] \} (-C_+ e^{-ky} + C_- e^{ky}) \rangle \quad (31) \quad 544$$

$$E_{2y}^m = \sum_n -\frac{k}{2\varepsilon_0(L_1 + L_2)} \langle \{ p_x [\sin(kx) - \sin(kx - 2kL_1 - \Delta\varphi)] \\ + p_y [\cos(kx) + \cos(kx - 2kL_1 - \Delta\varphi)] \} (-D_+ e^{-ky} + D_- e^{ky}) \rangle \quad (32) \quad 545$$

The complete solution for each constant is not shown here
546 due to their complexity; therefore, the coefficients are used in
547 order to reduce the equations of potentials and electric field.
548 However, these solutions can be directly obtained either
549 manually or using a mathematic software. 550

A similar mathematical derivation can be applied for a bow-
551 tie nanoantenna composed of three arms. The corresponding
552 results can be found in the [Supporting Information](#). 553

Numerical Simulations. The numerical results are
554 calculated using the commercial finite element analysis software
555 Comsol Multiphysics. The model of metal used in this work is
556 silver modeled as a Drude–Lorentz function with the form $\varepsilon_r =$
557 $\varepsilon_\infty - (\omega_p^2 / \omega(\omega - i\gamma)) + (\varepsilon_1 \omega_1^2) / (\omega_1^2 - \omega^2 + 2i\gamma\omega)$, with $\varepsilon_\infty =$
558 1.174, Drude plasma frequency $\omega_p = 13.6973 \times 10^{15}$ rad/s,
559 Lorentz plasma frequency $\omega_1 = 7.5398 \times 10^{15}$ rad/s, $\varepsilon_1 = 1.69$,
560 Drude damping constant $\gamma = 30.58 \times 10^{12}$ rad/s, and Lorentz
561 damping constant $\gamma_1 = 1839 \times 10^{12}$ rad/s. This function fits
562 Palik's experimental data.³⁶ The bow-tie antennas, with a total
563

length of $l' = 20$ nm, are immersed in a vacuum modeled as a two-dimensional square of $600 \text{ nm} \times 600 \text{ nm}$. In order to reduce undesirable reflections from the system, scattering boundary conditions (i.e., perfectly matched layers) have been applied to the boundaries of the square of the vacuum. The 2D TM point dipole used to illuminate the nanoantenna is modeled using two antiparallel in-plane magnetic currents with a separation of 5 pm. Also, an extremely refined mesh has been used with a maximum and minimum mesh size of 2 nm and 3 pm, respectively, for the box of the vacuum. For the bow-tie nanoantennas, a refined mesh 2 times smaller than the mesh used for the box of the vacuum is applied to ensure accurate results. For the systematic study shown in Figure 2c,g, the nonradiative power was evaluated by simulating in a frequency range from 300 to 1000 THz with a step of 20 THz for the following range of angles of aperture of the antennas: from 5° to 15° with a step of 0.25° , from 15° to 25° with a step of 0.5° , and from 25° to 45° with a step of 1° . This parametrical study was applied for both vertically and horizontally polarized dipole. With these parameters, the estimated time to solve each simulation (i.e., for one angle of aperture of the antennas with one polarization) was a mean of 90 min each.

ASSOCIATED CONTENT

Supporting Information

The Supporting Information is available free of charge on the ACS Publications website at DOI: 10.1021/acsphotonics.6b00232.

Additional information (PDF)

AUTHOR INFORMATION

Corresponding Author

*E-mail: m.navarro-cia@bham.ac.uk. Phone: +44(0) 1214144664. Fax: +44(0)1214144644.

Notes

The authors declare no competing financial interest.

ACKNOWLEDGMENTS

The authors would like to thank Prof. Sir J. Pendry for fruitful discussions. This work was supported in part by the Spanish Government under contract TEC2014-51902-C2-2-R. V.P.-P. is sponsored by Spanish Ministerio de Educación, Cultura y Deporte under grant FPU AP-2012-3796. M.B. is sponsored by the Spanish Government via RYC-2011-08221. Y.L. would like to acknowledge the funding support from NTU-A*STAR Silicon Technologies Centre of Excellence under the program grant no. 11235150003. M.N.-C. was supported by an Imperial College Junior Research Fellowship and is now supported by a Birmingham Fellowship.

REFERENCES

- (1) Balanis, C. A. *Antenna Theory: Analysis and Design*, 3rd ed.; John Wiley & Sons: Hoboken, NJ, 2005.
- (2) Pozar, D. M. *Microwave Engineering*; John Wiley & Sons: New York, 1998.
- (3) Novotny, L.; Hecht, B. *Principles of Nano-Optics*, 2nd ed.; Cambridge University Press: U.K., 2012.
- (4) Alù, A.; Engheta, N. Input Impedance, Nanocircuit Loading, and Radiation Tuning of Optical Nanoantennas. *Phys. Rev. Lett.* **2008**, *101*, 1–4.
- (5) Bharadwaj, P.; Deutsch, B.; Novotny, L. Optical Antennas. *Adv. Opt. Photonics* **2009**, *1*, 438.

- (6) Alu, A.; Engheta, N. Theory, Modeling and Features of Optical Nanoantennas. *IEEE Trans. Antennas Propag.* **2013**, *61*, 1508–1517.
- (7) Eggleston, M. S.; Messer, K.; Zhang, L.; Yablonovitch, E.; Wu, M. C. Optical Antenna Enhanced Spontaneous Emission. *Proc. Natl. Acad. Sci. U. S. A.* **2015**, *112*, 1704–1709.
- (8) Giannini, V.; Fernández-Domínguez, A. I.; Heck, S. C.; Maier, S. A. Plasmonic Nanoantennas: Fundamentals and Their Use in Controlling the Radiative Properties of Nanoemitters. *Chem. Rev.* **2011**, *111*, 3888–3912.
- (9) Nie, S. Probing Single Molecules and Single Nanoparticles by Surface-Enhanced Raman Scattering. *Science* **1997**, *275*, 1102–1106.
- (10) Anker, J. N.; Hall, W. P.; Lyandres, O.; Shah, N. C.; Zhao, J.; Van Duyne, R. P. Biosensing with Plasmonic Nanosensors. *Nat. Mater.* **2008**, *7*, 442–453.
- (11) Atwater, H. A.; Polman, A. Plasmonics for Improved Photovoltaic Devices. *Nat. Mater.* **2010**, *9*, 205–213.
- (12) Knight, M. W.; Sobhani, H.; Nordlander, P.; Halas, N. J. Photodetection with Active Optical Antennas. *Science* **2011**, *332*, 702–704.
- (13) Aouani, H.; Rahmani, M.; Navarro-Cia, M.; Maier, S. A. Third-Harmonic-Upconversion Enhancement from a Single Semiconductor Nanoparticle Coupled to a Plasmonic Antenna. *Nat. Nanotechnol.* **2014**, *9*, 290–294.
- (14) Bohren, C. F.; Huffman, D. R. *Absorption and Scattering of Light by Small Particles*; Wiley-VCH Verlag GmbH: Weinheim, Germany, 2007.
- (15) Massa, E.; Maier, S. A.; Giannini, V. An Analytical Approach to Light Scattering from Small Cubic and Rectangular Cuboidal Nanoantennas. *New J. Phys.* **2013**, *15*, 063013.
- (16) Luo, Y.; Pendry, J. B.; Aubry, A. Surface Plasmons and Singularities. *Nano Lett.* **2010**, *10*, 4186–4191.
- (17) Pendry, J. B.; Aubry, A.; Smith, D. R.; Maier, S. A. Transformation Optics and Subwavelength Control of Light. *Science* **2012**, *337*, 549–552.
- (18) Fernández-Domínguez, A. I.; Luo, Y.; Wiener, A.; Pendry, J. B.; Maier, S. A. Theory of Three-Dimensional Nanocrescent Light Harvesters. *Nano Lett.* **2012**, *12*, 5946–5953.
- (19) Pendry, J. B.; Fernández-Domínguez, A. I.; Luo, Y.; Zhao, R. Capturing Photons with Transformation Optics. *Nat. Phys.* **2013**, *9*, 518–522.
- (20) Aubry, A.; Pendry, J. B. Transformation Optics for Plasmonics. In *Active Plasmonics and Tunable Plasmonic Metamaterials*; Zayats, A., Maier, S. A., Eds.; John Wiley & Sons: Hoboken, NJ, 2013; pp 105–152.
- (21) DuHamel, R.; Isbell, D. Broadband Logarithmically Periodic Antenna Structures. *IRE Int. Conv. Rec.* **1957**, *5*, 119–128.
- (22) Carrel, R. The Characteristic Impedance of Two Infinite Cones of Arbitrary Cross Section. *IRE Trans. Antennas Propag.* **1958**, *6*, 243–245.
- (23) Ramo, S.; Whinnery, J. R.; Duzer, T. *Van. Fields and Waves in Communication Electronics*, 3rd ed.; John Wiley & Sons: U.K., 1965.
- (24) Heiblum, M.; Harris, J. H. Analysis of Curved Optical Waveguides by Conformal Transformation. *IEEE J. Quantum Electron.* **1975**, *11*, 75–83.
- (25) Xu, L.; Chen, H. Conformal Transformation Optics. *Nat. Photonics* **2014**, *9*, 1–8.
- (26) Yu, N.; Cubukcu, E.; Diehl, L.; Bour, D.; Corzine, S.; Zhu, J.; Höfler, G.; Crozier, K. B.; Capasso, F. Bowtie Plasmonic Quantum Cascade Laser Antenna. *Opt. Express* **2007**, *15*, 13272–13281.
- (27) Kinkhabwala, A.; Yu, Z.; Fan, S.; Avlasevich, Y.; Mullen, K.; E, M. Large Single-Molecule Fluorescence Enhancements Produced by a Bowtie Nanoantenna. *Nat. Photonics* **2009**, *3*, 654–657.
- (28) Hatab, N. A.; Hsueh, C. H.; Gaddis, A. L.; Retterer, S. T.; Li, J. H.; Eres, G.; Zhang, Z.; Gu, B. Free-Standing Optical Gold Bowtie Nanoantenna with Variable Gap Size for Enhanced Raman Spectroscopy. *Nano Lett.* **2010**, *10*, 4952–4955.
- (29) Ko, K. D.; Kumar, A.; Fung, K. H.; Ambekar, R.; Liu, G. L.; Fang, N. X.; Toussaint, K. C. Nonlinear Optical Response from Arrays of Au Bowtie Nanoantennas. *Nano Lett.* **2011**, *11*, 61–65.

- 691 (30) Navarro-Cia, M.; Maier, S. A. Broad-Band near-Infrared
692 Plasmonic Nanoantennas for Higher Harmonic Generation. *ACS*
693 *Nano* **2012**, *6*, 3537–3544.
- 694 (31) Aouani, H.; Navarro-Cia, M.; Rahmani, M.; Sidiropoulos, T. P.
695 H.; Hong, M.; Oulton, R. F.; Maier, S. A. Multiresonant Broadband
696 Optical Antennas As Efficient Tunable Nanosources of Second
697 Harmonic Light. *Nano Lett.* **2012**, *12*, 4997–5002.
- 698 (32) Sivis, M.; Duwe, M.; Abel, B.; Ropers, C. Extreme-Ultraviolet
699 Light Generation in Plasmonic Nanostructures. *Nat. Phys.* **2013**, *9*,
700 304–309.
- 701 (33) Roxworthy, B. J.; Bhuiya, A. M.; Yu, X.; Chow, E. K. C.;
702 Toussaint, K. C. Reconfigurable Nanoantennas Using Electron-Beam
703 Manipulation. *Nat. Commun.* **2014**, *5*, 4427.
- 704 (34) Hentschel, M.; Metzger, B.; Knabe, B.; Buse, K.; Giessen, H.
705 *Beilstein J. Nanotechnol.* **2016**, *7*, 111–120.
- 706 (35) Liu, M.; Lee, T.; Gray, S. K.; Guyot-sionnest, P.; Pelton, M.
707 Excitation of Dark Plasmons in Metal Nanoparticles by a Localized
708 Emitter. *Phys. Rev. Lett.* **2009**, *102*, 107401–4.
- 709 (36) Palik, E. D. *Handbook of Optical Constants of Solids*; Academic:
710 New York, 1985.
- 711 (37) Luo, Y.; Lei, D. Y.; Maier, S. A.; Pendry, J. B. Transformation-
712 Optics Description of Plasmonic Nanostructures Containing Blunt
713 Edges/corners: From Symmetric to Asymmetric Edge Rounding. *ACS*
714 *Nano* **2012**, *6*, 6492–6506.
- 715 (38) Luo, Y.; Lei, D. Y.; Maier, S. A.; Pendry, J. B. Broadband Light
716 Harvesting Nanostructures Robust to Edge Bluntness. *Phys. Rev. Lett.*
717 **2012**, *108*, 023901.
- 718 (39) Aubry, A.; Lei, D. Y.; Maier, S. A.; Pendry, J. B. Plasmonic
719 Hybridization between Nanowires and a Metallic Surface: A
720 Transformation Optics Approach. *ACS Nano* **2011**, *5*, 3293–3308.
- 721 (40) Giannini, V.; Fernández-Domínguez, A. I.; Sonnefraud, Y.;
722 Roschuk, T.; Fernández-García, R.; Maier, S. A. Controlling Light
723 Localization and Light-Matter Interactions with Nanoplasmonics.
724 *Small* **2010**, *6*, 2498–2507.